ROYAL SOCIETY OF CHEMISTRY

Check for updates

Direct mechanochemical synthesis of SrMoO₄: structural and luminescence properties

Maria Gancheva, [ID] *[a] Reni Iordanova,[a] Georgi Avdeev,[b] Iskra Piroeva[b] and Petar Ivanov[c]

In this study, the effects of ball milling conditions on the phase formation, symmetry of structural units and photoluminescence features of SrMoO₄ were investigated. A stoichiometric mixture of $SrCO_3$ and MoO_3 in a molar ratio of 1:1 was subjected to intense mechanical treatment in air using a planetary ball mill by applying two milling speeds: 500 and 850 rpm. The obtained samples were characterized by X-ray diffraction (XRD) analysis, scanning electron microscopy (SEM), Raman spectroscopy, infrared (IR) spectroscopy, UV-vis (UV-vis) diffuse reflectance spectroscopy and photoluminescence (PL) spectroscopy. The fast synthesis (1 h milling time) of tetragonal SrMoO₄ occurred at the higher milling speed of 850 rpm. A longer milling time (5 h) was needed to synthesize SrMoO₄ at a lower milling speed of 500 rpm. The average crystallite sizes of the as-prepared samples were 25 and 20 nm at 500 and 850 rpm, respectively. SEM analysis revealed that the mechanochemically produced SrMoO₄ sample contained a variety of particle shapes including hexagonal and polyhedral ones. Raman and IR spectroscopy results confirmed the formation of tetragonal SrMoO₄. UV-vis absorption spectra showed one peak at 230 nm, and the calculated optical band gaps of SrMoO₄ were 4.27 eV (5 h/500 rpm) and 4.34 eV (1 h/850 rpm). Photoluminescence (PL) spectra of both the samples exhibited blue emissions with a peak maximum at 400 (405) nm upon excitation at 325 nm wavelength. CIE coordinates of this mechanochemically synthesized SrMoO₄ were located in the blue region with different positions.

Introduction

Alkaline-earth metal molybdates have important technical and scientific applications in sensors,[1] catalysts,[2] scintillation detectors,[3] Raman scattering devices,[4] electrodes[5] and optical materials.[6–18] AMoO₄, where A is Ba, Ca, or Sr, is a well-known mixed oxide with a scheelite-type structure. In this crystal structure, the alkaline ions are coordinated with eight oxygen atoms and form an AO₈ polyhedron, and molybdate atoms are coordinated with four oxygen atoms in a tetrahedral symmetry. The MoO₄ polyhedra are connected to AO₈ through common corners.[19] Some of the important factors that are responsible for the properties of the inorganic mixed oxides are their crystal structure, morphology and method of synthesis. SrMoO₄ is one of the significant materials among the family of metal molybdates and has been subjected to deep investigations. The photocatalytic,[7,20] ferromagnetic,[8,21] electronic,[9,22] and optical properties of SrMoO₄ have been reported in the literature.[6,8,10–18,21,23] SrMoO₄

has a band gap in the range of 3.6–4.3 eV.[6–10,14,16,17,19,20,22,24,25] It exhibits strong photoluminescence at room temperature within the blue or green spectral regions owing to the electronic transition in the $[MoO_4]^{2-}$ complexes. The type of luminescence depends on the particle morphology, crystallite size, and defects. SrMoO₄ with sphere-like morphology shows emission at a lower wavelength around 378 nm.[11] SrMoO₄ with a lower crystallite size (17 nm) obtained *via* a microwave method exhibits emission at 410 nm.[12] SrMoO₄ with flower-like, peanut, dumbbell and notched sphere morphologies exhibits broader emission at 417 nm with different intensities.[13] SrMoO₄ with a microspherical shape and a crystallite size above 2 μm exhibits strong blue emissions at a higher wavelength (476 nm).[14] SrMoO₄ with irregular shapes of particles obtained by coprecipitation exhibits broad emission centered at 525 nm.[9] The emission of SrMoO₄ single crystals grown by the Chochralski method is located in the green spectral range with maximum at 515 nm.[15] The SrMoO₄ nanopowder with a crystallite size in the range from 32 to 42 nm also shows green emission at 540 nm.[16] According to the data reported in the literature, the additional emission band above 500 nm is attributed to Frenkel defects, trap centers or surface defects formed in crystal phases with a scheelite-type structure.[17,18,21,23,26–28] As a result, the emission spectrum is changed and may contain multiple emission bands.[17,18,28] Different methods of preparation have been applied for the

[a] Institute of General and Inorganic Chemistry, Bulgarian Academy of Sciences, Acad. G. Bonchev, bl.11, Sofia, Bulgaria. E-mail: m.gancheva@svr.igic.bas.bg; Tel: +359 2 979 3588

[b] Institute of Physical Chemistry, "Acad. Rostislaw Kaischew", Bulgarian Academy of Sciences, Acad. G. Bonchev, str., bl. 11, 1113 Sofia, Bulgaria

[c] Institute of Optical Materials and Technologies, "Acad. Jordan Malinowski", Acad. G. Bonchev, str., bl. 109, 1113 Sofia, Bulgaria

synthesis of $SrMoO_4$ crystals, powders or films: solid-state reactions,[6,10,22] the Chochralski method,[15] microwave-hydrothermal approaches,[16] hydrothermal synthesis,[24,25] solvothermal methods,[7,18] sol–gel routes,[11,22] co-precipitation methods,[8,9,13] microwave irradiation methods,[12] sonochemical methods[14] and microemulsion processes.[29] To date, the mechanochemical synthesis has not been used for the preparation of $SrMoO_4$. This approach was developed as an alternative technology for the preparation of various types of materials.[30–32] It is also called the "green method" due to the recognized advantages in terms of energy, time, and efficiency of resources.[33] Mechanochemical activation was used to accomplish the direct synthesis of different crystalline phases.[34–37] The chemical reaction during the ball milling process depends on several factors such as the nature of the initial reagents, the type of mills (horizontal rotary ball mill, planetary ball mill, vibration, shakier mill, *etc.*), milling speeds, milling time, ball-to-powder weight ratios (BPRs) and milling environments (dry or wet).[38] The milling speed has a decisive role for the chemical reaction at a constant BPR, number and diameter of balls, and milling chamber. The higher milling speed leads to rapid preparation of the desired phase.[39,40] Furthermore, the milling time has effects on the structure, particle morphology and properties. Longer milling time could lead to the formation of undesirable phases, agglomeration of the particles and more deformed structures.[40] The energy introduced during the milling process leads to the formation of different types of defects in the crystalline structure, which have influence on the properties of the final products.[41] In the literature, there are data for the mechanochemical synthesis of other members of scheelite-type structures such as $CaMoO_4$ and $BaMoO_4$ W. Janbua *et al.* used $Ca(NO_3)_2 \cdot 4H_2O$, $Ba(NO_3)_2$ and $Na_2MoO_4 \cdot 2H_2O$ as initial reagents, which were subjected to treatment using Vibro-Energy Grinding Mills (SEWGO-M-18-5) at room temperature for 1 to 120 min milling time.[42] Our group's focus is on how various ball milling conditions, *i.e.* speed, affect the direct synthesis of the inorganic compounds (AMO_4) with scheelite- and wolframite-type of structures at room temperature. On the basis of our previous investigations, we herein propose direct mechanochemical synthesis of $SrMoO_4$ using $SrCO_3$ and MoO_3 as precursors. The effect of milling speeds on the structural and optical properties was investigated.

Experimental

The stoichiometric ratio of $SrCO_3$ (Merck, purity 99.9%) and MoO_3 (Merck, purity 99.9%) is 1/1 corresponding to the $SrMoO_4$ phase, which was subjected to intensive mechanochemical activation. The high-energy ball milling of the initial mixture was carried out in a planetary ball mill (Fritsch–Premium line–Pulversette No 7) at milling speeds of 500 and 850 rpm. The activation was performed in an air atmosphere and the ball-to-powder weight ratio was 10/1. To minimize the temperature during milling, the process was realized for periods of 15 min, with rest periods of 5 min according to our previous studies.[34–36] SMO-I and SMO-II are the labels of the as-prepared samples, which were subjected to mechanochemical treatment at 500 and 850 rpm, respectively.

Characterization

The powder XRD patterns were acquired using a Bruker D8 Advance X-ray powder diffractometer (Karlsruhe, Germany) equipped with a CuKa radiation source (1.542 Å) and a LynxEye PSD detector. The lattice parameters (a, c), unit cell volume, lattice strain and crystallite size (D nm) were calculated using the HighScore plus 4.5 and ReX software (ReX v. 0.9.3 build ID 202308221535 (2023-08-22)). The experimental diffraction profiles were modeled using a pseudo-Voigt function and the following parameters: scale factors, background coefficients, atomic positions, lattice parameters, occupancy factors and asymmetry correction factors. The morphology of the samples was studied using a field-emission scanning electron microscope (JEOL IT800SHL) in both secondary and backscattered electron detectors placed in an in-chamber and in-lens microscope column. The Raman spectra were recorded using a *Via* Qontor Raman Confocal Microscope (Renishaw plc, Wotton-under-Edge, England, UK) at a laser wavelength of 532 nm (Nd:YAG-laser). The laser power on the sample was kept up to 1% of the nominal power, so no heating effects on the powder sample could be observed. The excitation light was focused and collected using a $50\times$ LWD objective lens. Infrared spectra were recorded in the range of $1200-400$ cm^{-1} using a Nicolet-320 FTIR spectrometer using KBr pellets at a spectral resolution of 2 nm. The diffuse-reflectance spectra were recorded using a Thermo Evolution 300 UV-vis Spectrophotometer equipped with a Praying Mantis device. Spectralon was used for taking background. The optical absorption band was calculated based on Tauc's equation: $\alpha h\nu = A(h\nu - E_g)^n$, where α is the absorption coefficient, A is the absorption constant, h is Plank's constant, and ν is the photon frequency.[43] In the mentioned relation, n represents the type of semiconductor charge transition. The value of n is related to the characteristics of the electronic transition type in the semiconductors: $n = 0.5$ for a direct allowed transition; $n = 2$ for an indirect allowed transition; $n = 3$ for an indirect forbidden transition; and $n = 3/2$ for a direct forbidden transition. $SrMoO_4$ is known as a direct transition metal oxide, and therefore, the value of $n = 0.5$. The PL emission spectra were recorded using a Horiba Fluorolog 3-22 TCS spectrophotometer (Longjumeau, France) equipped with a 450 W xenon lamp as the excitation source. The automated modular system with the highest sensitivity among those available on the market allows the measurement of light emission of practically any type of samples. All spectra were recorded at room temperature with the following instrumental parameters: increment: 10.00 nm; side entrance slit: 10.00 nm; side exit slit: 10.00 nm; and first intermediate slit: 10.00 nm.

Result and discussion

Phase formation and morphology of $SrMoO_4$

The phase evolution of the initial reactants as a function of milling speed (500 and 850 rpm) and time was monitored by XRD analysis (Fig. 1A and B) and Rietveld analysis (Fig. 2A and B). The XRD pattern of the initial mixture before ball milling treatment displays the principal peaks of orthorhombic MoO_3

(PDF-98-003-0258) and orthorhombic $SrCO_3$ (PDF-98-002-7293). The partial amorphization of reagents was detected after 1 h milling time at a lower milling speed of 500 rpm, which manifested the presence of amorphous halo. The XRD pattern shows that all diffraction lines were widened and their intensity decreased. New diffraction lines corresponding to the tetragonal $SrMoO_4$ (PDF-98-017-3120) were observed when the milling time was increased by up to three hours. However, the presence of low-intensity peaks at 26 and 36°, which are typical for initial MoO_3 and $SrCO_3$, suggests that more milling energy is required to finish the reaction. The pure phase of tetragonal $SrMoO_4$ was formed after 5 hours of milling time at a milling speed of

500 rpm, the diffraction peaks are indexed and show that the structure belongs to the space group $I4_1/a$ (Fig. 1A). We reported similar results for other scheelite-type structures synthesized by mechanochemical activation.[35,36] It is well known that the higher milling energy facilitates the formation of a more ordered crystal structure with improved properties. The milling speed of 850 rpm led to faster reactions between the initial reagents. The principal diffraction lines of tetragonal $SrMoO_4$ are observed after 30 min of milling time (Fig. 1B). The additional ball milling up to 60 min milling time did not lead to any change in the phase composition of $SrMoO_4$. The phase formation of $SrMoO_4$ can be achieved by the following paths: by the formation of intermediate amorphous state at a lower milling speed (500 rpm) and direct and rapid synthesis at a higher milling speed (850 rpm). This result proves that mechanochemical activation is a suitable method for the preparation of nanocrystalline $SrMoO_4$. The Rietveld refinement analysis of the SMO-I and SMO-II samples was performed using the HighScore plus 4.5 and ReX software (Fig. 2A and B). There are several factors for the evaluation of XRD pattern fitness. One of the main parameters is the goodness of fit (GOF), $GOF^2 = (R_{wp}/R_{exp})^2$, and it is 1.45 for SMO-II and 1.26 for SMO-I, indicating a good fit to the experimental data. The calculated values of the lattice parameters (a and c) and the unit cell volume were found to increase with the increasing milling time at a lower speed (Table 1). The obtained values of structural parameters of SMO-I (5 h/500 rpm) are closer of the standard value (PDF-98-017-3120). This fact can be explained by better crystallinity due to longer time of synthesis. The calculated value of the unit cell of SMO-II (1 h/850 rpm) is lower than that of SMO-I (5 h/500 rpm). The reduction of unit cell volume can be caused from a compressive strain due to the higher milling energy induced at a higher speed. R. Künzel *et al.* reported almost the same values of unit cell of $SrMoO_4$ prepared by coprecipitation and subjected to thermal treatment and electron irradiations.[21] They explain this fact with intrinsic defects such as oxygen vacancies, interstitial strontium ions, interstitial oxygen ions, and more complicated structures such as defect clusters or Frenkel defects. We believe that the higher milling speed and short time of synthesis produce the Frenkel defects, which is in good agreement with photoluminescence spectrum (Fig. 7). We chose the diffraction peak at the 112 plane to determine the crystallite sizes (D, nm) and microstrains (ε, %) of mechanochemically synthesized SMO-I (1 h/500 rpm) and SMO-II (1 h/850 rpm). The calculated crystallite size of SMO-II is lower (20 nm) than the crystallite sizes of SMO-I (25 nm). The as-milled samples have relatively reduced D values than those of the as-prepared $SrMoO_4$ materials obtained by the microwave-hydrothermal synthesis,[16] solvothermal[7] and sol–gel methods.[44] The value of the macrostrains (ε, %) increases with the increase in milling speed. There are slight differences in the Mo–O length bond of SMO-I and SMO-II samples, which is an indication for compressing the Mo–O bonds using the higher milling speed (850 rpm). The microstructure of SMO-I and SMO-II samples synthesized under different mechanochemical treatments for long and short milling time periods were investigated, and are shown in Fig. 3. The SEM images at low and
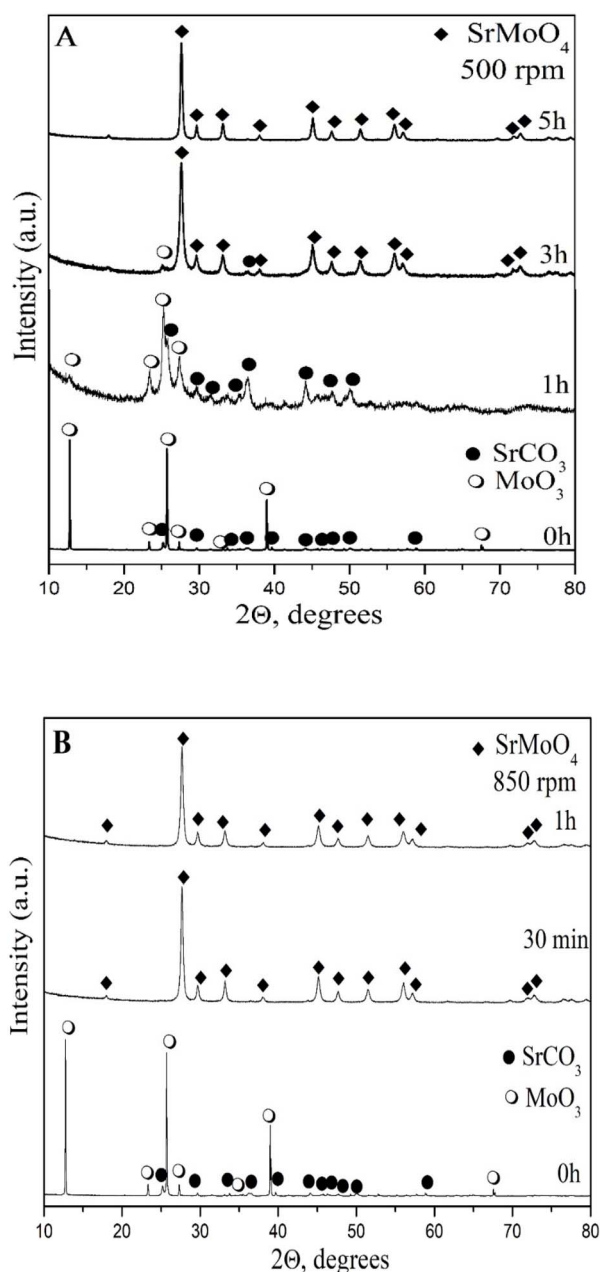

Fig. 1 XRD patterns of the mixture from $SrCO_3$ and MoO_3 mechanochemically activated at 500 rpm (A) and 850 rpm (B).
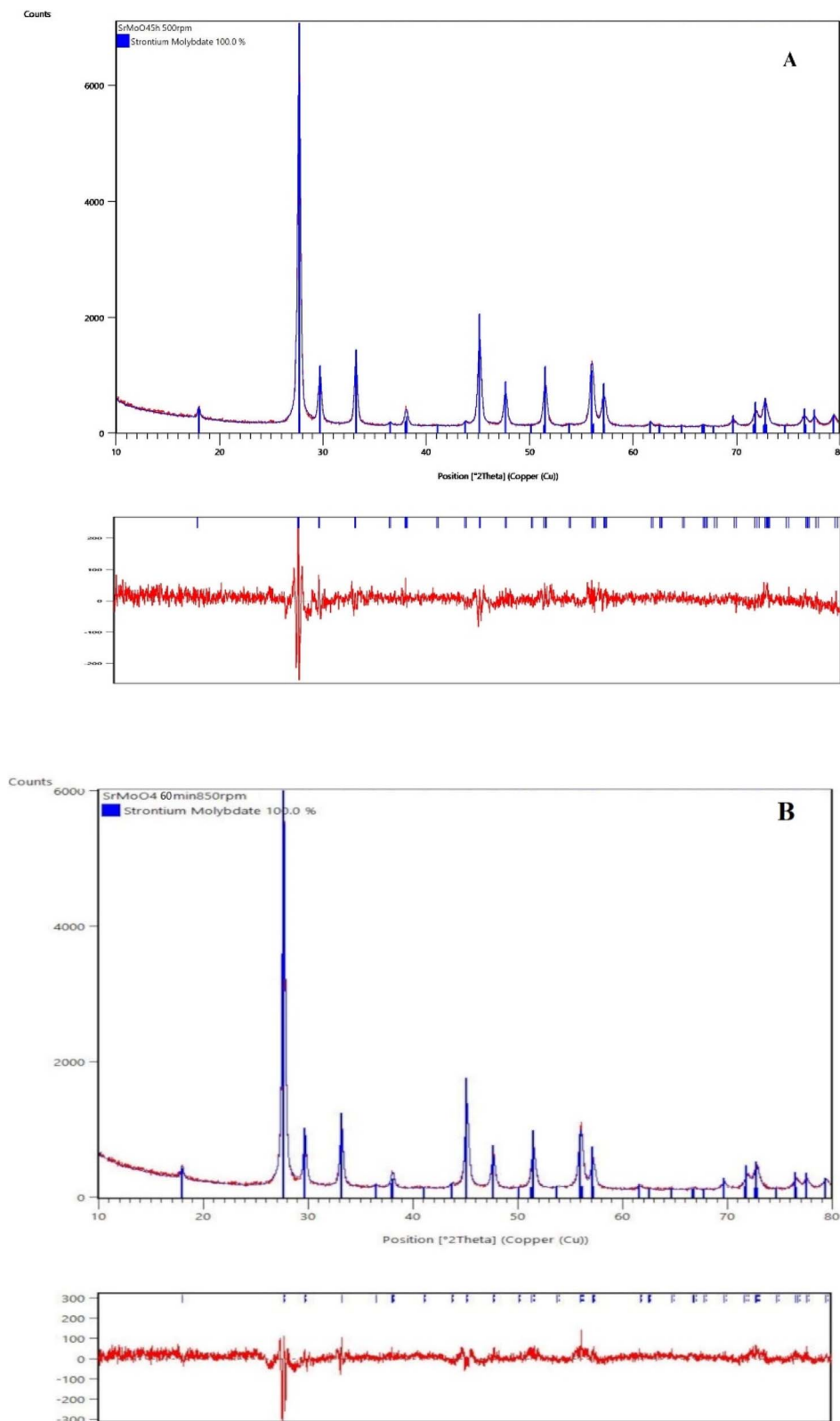
Fig. 2 Results of Rietveld refinements of the XRD patterns of mechanochemically synthesized SMO-I (5 h/500 rpm) (A) and SMO-II (1 h/850 rpm) (B) samples.

high magnifications (50 000 (a, c) and 80 000 (b, d)) show the presence of grains having polyhedral shapes with nano sizes. The particle sizes are in the range of less than 10 nm to 100 nm.

The small hexagonal particles were also observed for mechanochemically prepared SMO-I and SMO-II. Fig. 4 presents the particle size distributions of both the samples derived from the

© 2025 The Author(s). Published by the Royal Society of Chemistry

Table 1 Unit cell parameters (*a*, *b* and *c*), unit cell volume, crystallite size, lattice microstrain values and average distance of mechanochemically synthesized samples

| Unit cell parameters	SrMoO$_4$ – I, 5 h, 500 rpm	SrMoO$_4$ – II, 1 h, 850 rpm	SrMoO$_4$ (PDF#98-017-3120)
$a = b$ [Å], c [Å]	5.3918(2), 12.0176(6)	5.3896(2), 12.0107(6)	5.3950, 12.0260
Unit cell volume [Å^3]	349.36(1)	348.89(3)	350.03
Crystallites size [nm] at 112 plane	25(1)	20(7)	n.a
Lattice strain ε (%) at 112 plane	0.638	0.740	n.a
Average distance [Å]	Mo–O, 1.777; Sr–O, 2.574	Mo–O, 1.757; Sr–O, 2.572	n.a
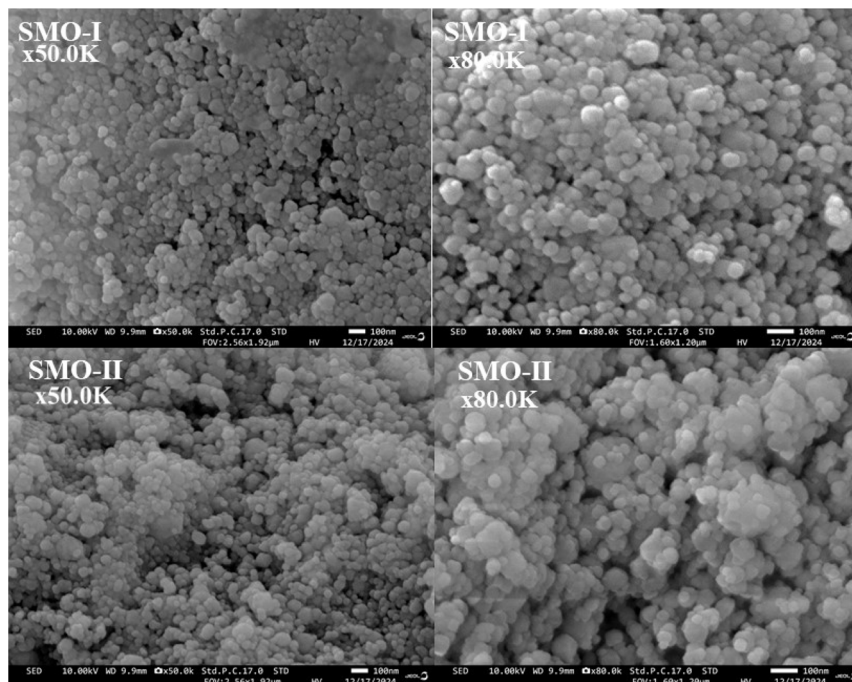
Fig. 3 SEM micrographs of mechanochemically synthesized SMO-I (5 h/500 rpm) and SMO-II (1 h/850 rpm) samples at different magnifications.

SEM images. The average particle size of SMO-I and SMO-II is 76 and 72 nm, respectively.

Structural investigation

Raman and IR spectroscopy gives information regarding the vibrations of the main structural units in the crystal phases. From the literature data on crystal phases with scheelite-type structures and group-theory analysis, it was found that SrMoO$_4$ has 26 different vibrations as follows: $3A_g + 5A_u + 5B_g + 3B_u + 5 E_g + 5E_u$. The A and B modes are non-degenerate, whereas the E modes are doubly degenerate.[45,46] A_g, B_g, and E_g are Raman active, while Au and Eu are active in the IR spectra. Therefore, 13 Raman vibrations, $3A_g + 5B_g + 5 E_g$, are registered for SrMoO$_4$. The molecular ionic group $[MoO_4]^{2-}$ with a strong covalent bond, Mo–O, is a peculiarity of the scheelite-type structure. Owing to weak coupling between the ionic group and metal cation Sr^{2+}, the phonon modes in the Raman spectra of the SrMoO$_4$ crystal can be divided into two groups: internal and external vibrations. The internal mode is related to the $[MoO_4]^{2-}$ molecular group with a stationary mass center. The external vibrations or lattice phonons are associated with the motion of the Sr^{2+} cation and the rigid molecular units.[6,7,9,12,17,45]

The Raman spectra of SMO-I and SMO-II were recorded in the range from 100 to 1000 cm^{-1}, and are shown in Fig. 5A. It can be seen from the figure that both spectra contain typical vibrations
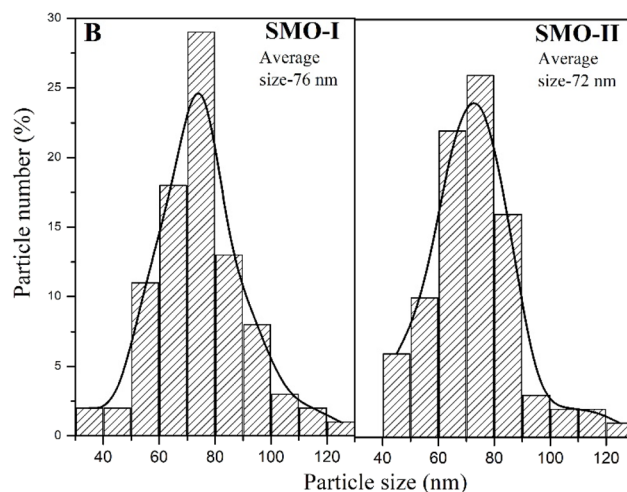
Fig. 4 Particle size distribution histogram of mechanochemically synthesized SMO-I (5 h/500 rpm) and SMO-II (1 h/850 rpm) samples.

of $SrMoO_4$. The most intensive band at 886 cm^{-1} is assigned to the symmetric stretching vibration ν_1 (A_g) of $[MO_4]^{2-}$ tetrahedral units. The peaks at 844 and 795 cm^{-1} are assigned to the antisymmetric stretching ν_3 (B_g and E_g) vibration of the same units. The ν_4 (E_g and B_g) antisymmetric bending modes was registered at 380 and 366 cm^{-1} while the peak at 326 cm^{-1} is a result of ν_1 (A_g) symmetric bending modes of vibration $[MoO_4]^{2-}$.[12] The free rotational mode ν_{fr} (A_g) was detected at 180 cm^{-1}, while the external ν_{ext} mode was observed at 136 cm^{-1}. These results are in agreement with those reported in the literature.[7,8,10,16,24,28,45–47] More information about the deformation of $[MoO_4]^{2-}$ structural units were obtained by infrared spectroscopy (Fig. 5B). Both spectra are similar, and there is an intensive band in the range of 800–900 cm^{-1} (with a shoulder) and one weak band at 405 cm^{-1}. In the IR spectrum of SMO-II, obtained at a high milling speed of 850 rpm, one broader band at 830 cm^{-1} was observed. This band is assigned to the ν_3 vibration of the $[MO_4]^{2-}$ structural units, building the crystalline structure of $SrMoO_4$.[5,12,24,46] It is obvious that this absorption band is shifted to a lower wavenumber at 815 cm^{-1}, and a weak shoulder at 850 cm^{-1} appears in the IR spectrum of SMO-I prepared at a lower milling speed (500 rpm). The XRD analysis revealed that the Mo–O bond distance in SMO-I is longer (Table 1); therefore, the absorption band position is changed. The appearance of the shoulder at 850 cm^{-1} is attributed to the elimination of the ν_3 vibration degeneracy of MoO_4 tetrahedra with different local symmetries.[35] In our previous study, it has been confirmed that prolonged milling time leads to the deformation of $[MoO_4]^{2-}$ structural units.[35,36] This result indicates that a more symmetric $[MO_4]^{2-}$ entity was formed at a higher milling speed (850 rpm). The weak absorption band at 405 cm^{-1} in both IR spectra was registered, which was assigned to the strontium–oxygen (Sr–O) stretching mode.[5]

Optical properties

The optical properties of $SrMoO_4$ were investigated by UV-vis diffuse reflectance and the photoluminescence (PL) techniques. The diffuse reflectance spectra were transformed into absorption spectra by the Kubelka–Munk function.[48] In Fig. 6A, an absorption peak of SMO-I and SMO-II is observed at 230 nm. This band is attributed to the charge transfer from oxygen into the central molybdenum atom inside the $[MoO_4]^{2-}$ groups.[7,14,24,25] However, a slight increase in the intensity was observed for SMO-I sample. The high absorbance in the UV region suggests that the $SrMoO_4$ phase exhibits a strong PL signal. Based on Tauc's equation, the values of the band gap (E_g) of both samples were determined. The calculated optical band gap values for SMO-I and SMO-II are 4.27 and 4.34 eV, respectively (Fig. 6B). The longer milling process improves the crystallinity, increases the average crystallite size, and decreases defects, therefore the band gap energy decreases. The value of the bandgap was found to increase with the increase in milling speed and decrease in the crystallite size. The variation in the values can be attributed to the presence of higher defects in the crystal structure that is connected with a higher microstrain (Table 1).[10] The band gap of the mechanochemically
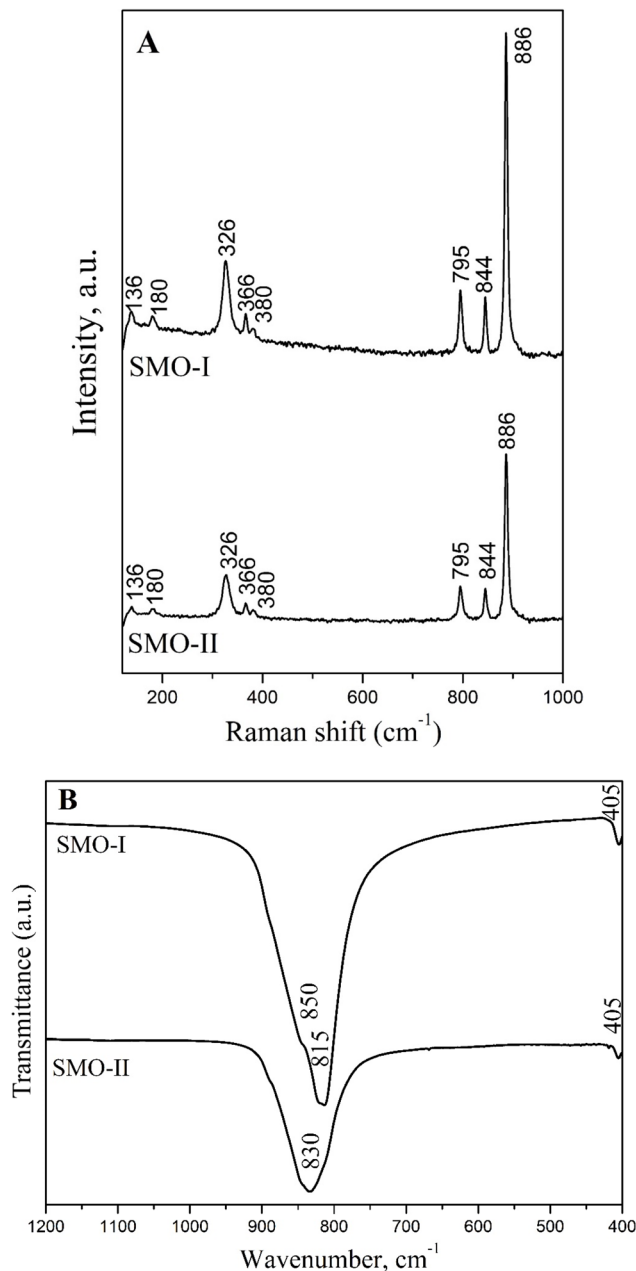

Fig. 5 Raman (A) and infrared (B) spectra of mechanochemically synthesized SMO-I (5 h/500 rpm) and SMO-II (1 h/850 rpm) samples.

synthesized $SrMoO_4$ is higher than that of $SrMoO_4$ prepared *via* solid-state reactions,[6,10] solvothermal methods,[7] sonochemical routes,[14] hydrothermal methods,[24,25] microemulsion processes[29] and coprecipitation.[46]

The room-temperature photoluminescence (PL) emission spectra of mechanochemically synthesized $SrMoO_4$ nanoparticles are shown in Fig. 7. The observed maximum peak at 400 (405 nm) of both samples is attributed to charge-transfer transitions within the $[MoO_4]^{2-}$ groups. The differences in the number of peaks, intensity of main peak and profile of the curves were observed. The photoluminescence of SMO-II shows intense blue emissions at 400 nm and weak yellow emissions at
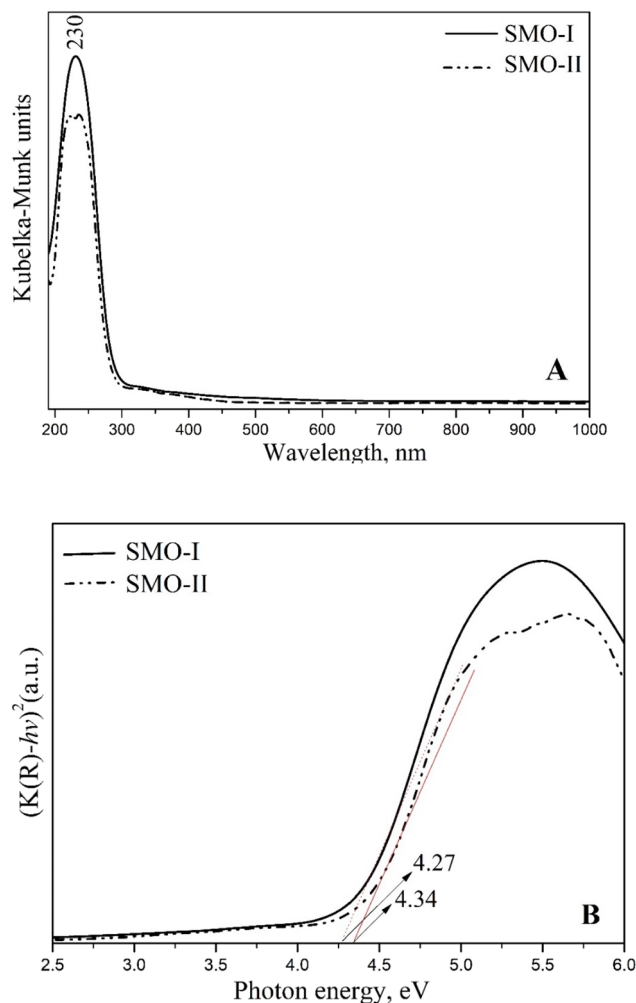
Fig. 6 Transformed Kubelka–Munk (from diffuse reflectance spectra) function (A) and Tauc plot (B) of mechanochemically synthesized SMO-I (5 h/500 rpm) and SMO-II (1 h/850 rpm) samples.
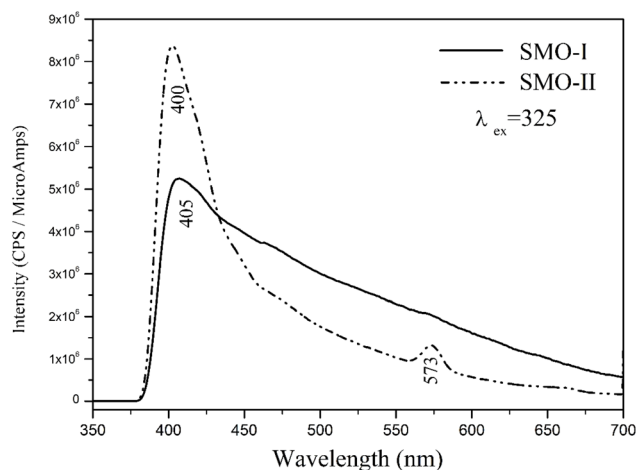

Fig. 7 Photoluminescence emission spectra of mechanochemically synthesized SMO-I (5 h/500 rpm) and SMO-II (1 h/850 rpm) samples.
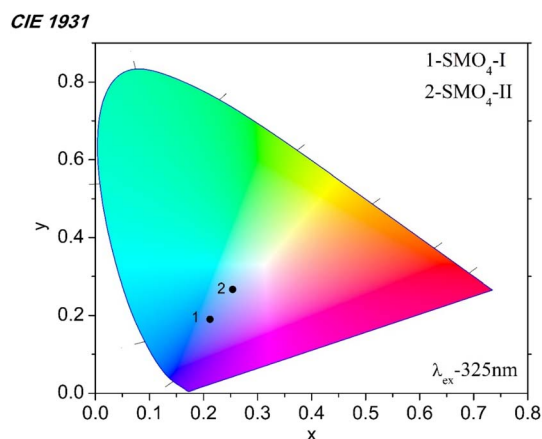

Fig. 8 CIE chromaticity diagram of mechanochemically synthesized SMO-I (5 h/500 rpm) and SMO-II (1 h/850 rpm) samples.

573, nm compared to SMO-I which shows emissions only at 405 nm. According to the literature data, the emission peak above 500 nm is attributed to the presence of Frenkel defects in the crystal structures (oxygen ion shifted to the inter-site position with simultaneous creation of vacancies).[17,18,23,26] Alternatively, the peak at 573 nm disappeared in the PL spectrum of SMO-I, which implies that a longer milling time at lower milling speeds (500 rpm) leads to the formation of the crystal phase without the Frenkel defects. The emission profile of SMO-I is broader with a lower intensity than that for SMO-II. A similar photoluminescence curve was reported for $SrMoO_4$ prepared by a microwave-irradiation method,[12] a precipitation method[13] and a microemulsion method.[29] The photoluminescence spectra show a notable change in the intensity of the samples, suggesting that SMO-II possesses more defects.[49] M. A. Gomes et al.,[49] concluded that the large emission band has contributions from different defects and the type of defect formed and its quantity depends strongly on how the sample was prepared and treated. We established a higher milling speed and a short milling time, which lead to the formation of Frenkel defects and

stronger emissions. The other reasons for higher emissions of SMO-II (1 h/850 rpm) are more symmetrical $[MoO_4]^{2-}$ units and lower crystallite sizes.[35,47]

We investigated the emission color of the mechanochemically synthesized samples using the 1931 CIE (Commission Internationale de L'Eclairage) system. The CIE coordinates were calculated, and their position is shown in the CIE diagram (Fig. 8). The CIE coordinates (x, y) of SMO-I are 0.212 and 0.190, while those of SMO-II are 0.254 and 0.267. It is clear that the emission color changes from blue to light blue depending on the milling time. The formation of the Frenkel defects at a higher milling speed (850 rpm) has influences on the emission color of the material.

Conclusions

In this study, we evidenced that the milling speeds have a strong effect on the synthesis time and optical properties of nanocrystallite $SrMoO_4$. The X-ray diffraction analysis, infrared spectroscopy and photoluminescence spectroscopy revealed

that higher milling speeds led to the formation of $SrMoO_4$ with smaller crystallite sizes, symmetrical MoO_4 units, strong photoluminescence and formation of the Frenkel-type defects. A lower milling speed produces a crystalline phase with higher crystallite sizes, more deformed MoO_4 units and wider photoluminescence emissions. The particle morphologies of $SrMoO_4$ are very similar and consist of polyhedral and hexagonal grains. Strong blue and weak yellow emissions were observed for $SrMoO_4$ obtained at a higher ball milling speed (1 h/850 rpm). Only blue emissions were detected for $SrMoO_4$ synthesized at a lower ball milling speed (5 h/500 rpm). The emission intensity was found to depend on the presence of defects and the symmetry of MoO_4 in the $SrMoO_4$ structure. It was established that depending on the applied activation speed, materials with different shades of emission colors can be obtained.

Data availability

The data and results are available in the article.

Author contributions

To this work according to CRediT standardised contribution descriptions are as follows: Maria Gancheva (conceptualization, investigation, visualization, and writing-original draft), Reni Iordanova (supervision, methodology, and writing-review & editing), Georgi Avdeev (XRD analysis and software), Iskra Piroeva (SEM investigations) and Petar Ivanov (PL investigation and data curation).

Conflicts of interest

There are no conflicts to declare.

Acknowledgements

Notes and references

1 A. K. Soni, A. Kumari and V. K. Rai, *Sens. Actuators, B*, 2015, **216**, 64–71.

2 R. Georgieva, M. Gancheva, G. Ivanov, M. Shipochka, P. Markov, D. Nihtianova, R. Iordanova and A. Naydenov, *React. Kinet., Mech. Catal.*, 2021, **132**, 811–827.

3 V. B. Mikhailik, Y. Elyashevskyi, H. Kraus, H. J. Kim, V. Kapustianyk and M. Panasyuk, *Nucl. Instrum. Methods Phys. Res., Sect. A*, 2015, **792**, 1–5.

4 H. Yu, Z. Li, A. J. Lee, J. Li, H. Zhang, J. Wang, H. M. Pask, J. A. Piper and M. Jiang, *Opt. Lett.*, 2011, **36**, 579–581.

5 A. Sathiyan, S. Rajkumar, S. Dhineshkumara and J. Princy Merlin, *J. Ind. Eng. Chem.*, 2024, **129**, 521–530.

6 C. L. Ranganatha, H. S. Lokesha, K. R. Nagabhushana and B. S. Palakshamurthy, *J. Alloys Compd.*, 2023, **962**, 171061–1701070.

7 J. Luo, X. Bai, Q. Li, X. Yu, C. Li, Z. Wang, W. Wu, Y. Liang, Z. Zhao and H. Liu, *Nano Energy*, 2019, **66**, 104187–104196.

8 M. Muralidharan, V. Anbarasu, A. Elaya Perumal and K. Sivakuma, *J. Mater. Sci.: Mater. Electron.*, 2016, **27**, 2545–2556.

9 I. C. Nogueira, L. S. Cavalcante, P. F. S. Pereira, M. M. de Jesus, J. M. Rivas Mercury, N. C. Batista, M. S. Li and E. Longo, *J. Appl. Crystallogr.*, 2013, **46**, 1434–1446.

10 A. Shandilya, R. S. Yadav, A. K. Gupta and K. Sreenivas, *Mater. Chem. Phys.*, 2021, **264**, 124441–124456.

11 H. Gao, Y. Wang, Q. Gao, X. Pan, S. Wang, H. Yang, C. Chen, Y. Wang, L. Fang and Z. Yi, *Optik*, 2020, **241**, 167040–167053.

12 T. Thongtem, A. Phuruangrat and S. Thongtem, *J. Nanopart. Res.*, 2010, **12**, 2287–2294.

13 G. Xing, Y. Li, Y. Li, Z. Wu, P. Sun, Y. Wang, C. Zhao and G. Wu, *Mater. Chem. Phys.*, 2011, **127**, 465–470.

14 J. Zhang, R. Li, L. Liu, L. Li, L. Zou, S. Gan and G. Ji, *Ultrason. Sonochem.*, 2014, **21**, 1736–1744.

15 S. B. Mikhrin, A. N. Mishin, A. S. Potapov, P. A. Rodnyi and A. S. Voloshinovskii, *Nucl. Instrum. Methods Phys. Res., Sect. A*, 2002, **486**, 295–297.

16 J. C. Sczancoski, L. S. Cavalcante, M. R. Joya, J. A. Varela, P. S. Pizani and E. Longo, *Chem. Eng. J.*, 2008, **140**, 632–637.

17 C. Shivakumara and R. Saraf, *Opt. Mater.*, 2015, **42**, 178–186.

18 S. Lei, X. Peng, X. Li, Z. Liang, Y. Yang, B. Cheng and Y. Xiao, *Mater. Res. Bull.*, 2011, **46**, 601–608.

19 A. W. Sleght, *Acta Crystallogr., Sect. B*, 1972, **28**, 2899–2904.

20 Z. F. Yao, Z. X. Dai, Z. J. Zhang, G. H. Zheng and X. Xu, *Appl. Organomet. Chem.*, 2019, **32**, 4648–4658.

21 R. Künzel, C. M. S. Feldhaus, Y. O. F. Suzuki, F. F. Ferreira, V. G. Paula, L. C. Courrol, N. K. Umisedo, E. M. Yoshimura, E. Okuno and A. P. A. Marques, *J. Magn. Magn. Mater.*, 2022, **562**, 169761–169774.

22 C. Thirmal, S. D. Ramarao, L. Srinivasa Rao and V. R. K. Murthy, *Mater. Res. Bull.*, 2022, **146**, 111618–111624.

23 F. Zhang, M. Y. Sfeir, J. A. Misewich and S. S. Wong, *Chem. Mater.*, 2008, **20**, 5500–5512.

24 R. Künzel, N. K. Umisedo, E. Okuno, E. M. Yoshimura and A. P. A. Marques, *Ceram. Int.*, 2020, **46**, 15018–150026.

25 V. Elakkiya and S. Sumathi, *Mater. Lett.*, 2020, **263**, 127246–127250.

26 J. H. Ryu, B. G. Choi, J. W. Yoon, K. B. Shim, K. Machi and K. Hamada, *J. Lumin.*, 2007, **124**, 67–70.

27 D. A. Spassky, V. Nagirnyi, V. V. Mikhailin, A. E. Savon, A. N. Belsky, V. V. Laguta, M. Buryi, E. N. Galashov, V. N. Shlegel, I. S. Voronina and B. I. Zadneprovski, *Opt. Mater.*, 2013, **35**, 2465–2472.

28 S. M. V. Paradelas, R. F. Gonçalves, F. V. Motta, R. C. Lima, M. S. Li, E. Longo and A. P. A. Marques, *J. Lumin.*, 2017, **192**, 818–826.

29 J. Liu, J. Ma, B. Lin, Y. Ren, X. Jiang, J. Tao and X. Zhu, *Ceram. Int.*, 2008, **34**, 1557–1560.

30 T. Friščić, C. Mottillo and H. M. Titi, *Angew. Chem., Int. Ed.*, 2020, **59**, 1018–1029.

31 F. Palazon, Y. E. Ajjourt, P. Sebastia-Luna, S. Lauciello, L. Monna and H. J. Bolink, *J. Mater. Chem. C*, 2019, **7**, 11406–11410.

32 K. K. F. Barbosa, D. Aristizábal-Giraldo, J. M. Osorio-Guillén, J. J. S. Acuña and F. F. Ferreira, *RSC Mechanochemistry*, 2024, **1**, 69–77.

33 K. J. Ardila-Fierro and J. G. Hernández, *ChemSusChem*, 2021, **14**, 1–19.

34 Y. Dimitriev, M. Gancheva and R. Iordanova, *J. Alloys Compd.*, 2012, **519**, 161–166.

35 M. Gancheva, I. Koseva, R. Iordanova, G. Avdeev, G. Burdina and P. Ivanov, *Materials*, 2023, **16**, 7025–7036.

36 M. Gancheva, I. Koseva, R. Iordanova, P. Tzvetkov and P. Ivanov, *Materials*, 2024, **17**, 3724–3738.

37 R. D. McAuliffe, G. E. Kamm, M. J. McDermott, R. P. Hermann, N. Vasquez-Garcia, R. L. Sacci, K. A. Persson, K. W. Chapman and G. M. Veith, *Inorg. Chem.*, 2023, **62**, 3358–3367.

38 C. Liu, M. Wu, Y. Liu, Z. Lu, Y. Yang, S. Shia and Y. Gyan, *Mater. Res. Bull.*, 2018, **99**, 436–443.

39 M. Mancheva, R. Iordanova and Y. Dimitriev, *J. Alloys Compd.*, 2011, **509**, 15–20.

40 C. Jiten, M. Rawat, A. Bhattacharya and K. C. Singh, *Mater. Res. Bull.*, 2017, **90**, 162–169.

41 Y. Reséndiz-Trejo, F. Sánchez-De Jesús, L. G. Betancourt-Cantera, M. I. Reyes-Valderrama, C. A. Cortés-Escobedo and A. M. Bolarín-Miró, *Ceram. Int.*, 2024, **50**, 53533–53543.

42 W. Janbua, T. Bongkarn, W. Vittayakorn and N. Vittayakorn, *Ceram. Int.*, 2017, **43**(1), S435–S443.

43 J. Tauc, *Mater. Res. Bull.*, 1970, **5**, 721–729.

44 S. W. Park, B. K. Moon, J. H. Jeong, J. S. Bae and J. H. Kim, *Mater. Res. Bull.*, 2015, **70**, 403–411.

45 S. P. S. Porto and J. F. Scott, *Phys. Rev.*, 1967, **157**, 716–719.

46 T. Thongtern, S. Kungwankunakon, B. Kuntalue, A. Phuruangrat and S. Thongtem, *J. Alloys Compd.*, 2010, **506**, 475–481.

47 A. Hallaouia, A. Taoufyqa, M. Arab, B. Bakiz, A. Benlhachemi, L. Bazzi, J.-C. Valmalettea, S. Villain, F. Guinneton and J.-R. Gavarri, *Mater. Res. Bull.*, 2016, **79**, 121–132.

48 W. E. Vargas and G. A. Niklasson, *Appl. Opt.*, 1997, **36**, 5580–5586.

49 M. A. Gomes, L. F. A. Domingos, N. S. Santos, A. B. Andrade, D. M. Pickup, A. V. Chadwick, M. E. G. Valerio and Z. S. Macedo, *J. Alloys Compd.*, 2024, **983**, 173795–173804.